remote sensing

MDPI

Article

Robust Satellite Techniques (RSTs) for SO_2 Detection with MSG-SEVIRI Data: A Case Study of the 2021 Tajogaite Eruption

Rui Mota [1], Carolina Filizzola [2], Alfredo Falconieri [2], Francesco Marchese [2], Nicola Pergola [2], Valerio Tramutoli [3], Artur Gil [1] and José Pacheco [1,*]

[1] Research Institute for Volcanology and Risk Assessment (IVAR), University of the Azores, 9500-321 Ponta Delgada, Portugal; rui.ms.mota@uac.pt (R.M.); artur.jf.gil@uac.pt (A.G.)
[2] Institute of Methodologies for Environmental Analysis, National Research Council, Tito Scalo, 85050 Potenza, Italy; carolina.filizzola@cnr.it (C.F.); alfredo.falconieri@cnr.it (A.F.); francesco.marchese@cnr.it (F.M.); nicola.pergola@cnr.it (N.P.)
[3] School of Engineering, University of Basilicata, 85100 Potenza, Italy; valerio.tramutoli@unibas.it
* Correspondence: jose.mr.pacheco@azores.gov.pt

Highlights

What are the main findings?

- This study evaluates a novel RST configuration tailored for volcanic SO_2 detection using SEVIRI data.
- The proposed configuration detected SO_2 on ~81% of eruption days, with high precision (~79%) and very low false positives (<2%)

What is the implication of the main finding?

- The RST method can provide a robust, near-real-time monitoring tool, complementing UV-based products that are more sensitive but with a lower temporal resolution.
- The approach demonstrates strong potential for operational use with MTG/FCI, contributing volcanic hazard monitoring in future eruptions.

Abstract

Volcanic gas emissions, particularly sulfur dioxide (SO_2), are crucial for volcano monitoring. SO_2 has a significant impact on air quality, the climate, and human health, making it a critical component of volcano monitoring programs. Additionally, SO_2 can be used to assess the state of a volcano and the progression of an individual eruption and can serve as a proxy for volcanic ash. The Tajogaite La Palma (Spain) eruption in 2021 emitted large amounts of SO_2 over 85 days, with the plume reaching Central Europe. In this study, we present the results achieved by monitoring Tajogaite SO_2 emissions from 19 September to 31 October 2021 at different acquisition times (i.e., 10:00 UTC, 12:00 UTC, 14:00 UTC, and 16:00 UTC). An optimized configuration of the Robust Satellite Technique (RST) approach, tailored to volcanic SO_2 detection and exploiting the Spinning Enhanced Visible and InfraRed Imager (SEVIRI) channel at an 8.7 μm wavelength, was used. The results, assessed by means of a performance evaluation compared with masks drawn from the EUMETSAT Volcanic Ash RGB, show that the RST product identified volcanic SO_2 plumes on approximately 81% of eruption days, with a very low false-positive rate (2% and 0.3% for the mid/low and high-confidence-level RST products, respectively), a weighted precision of ~79%, and an F1-score of ~54%. In addition, the comparison with the Tropospheric Monitoring Instrument (TROPOMI) S5P Product Algorithm Laboratory (S5P-PAL) L3 grid Daily SO_2 CBR product shows that RST-SEVIRI detections were mostly associated with SO_2 plumes having a column density greater than 0.4 Dobson Units (DU). This study gives rise to some

Academic Editor: Mike Wolff

Received: 30 April 2025
Revised: 16 September 2025
Accepted: 18 September 2025
Published: 1 October 2025

Citation: Mota, R.; Filizzola, C.; Falconieri, A.; Marchese, F.; Pergola, N.; Tramutoli, V.; Gil, A.; Pacheco, J. Robust Satellite Techniques (RSTs) for SO_2 Detection with MSG-SEVIRI Data: A Case Study of the 2021 Tajogaite Eruption. *Remote Sens.* **2025**, *17*, 3345. https://doi.org/10.3390/rs17193345

interesting scenarios regarding the near-real-time monitoring of volcanic SO_2 by means of the Flexible Combined Imager (FCI) aboard the Meteosat Third-Generation (MTG) satellites, offering improved instrumental features compared with the SEVIRI.

Keywords: SEVIRI; SO_2 detection; RST algorithm; volcanic clouds; volcanic monitoring; Tajogaite

1. Introduction

Volcanic gas emissions are a key aspect of volcano monitoring worldwide, among which H_2O, CO_2, and SO_2 are the most prevalent [1,2]. In particular, SO_2 has a significant impact on air quality [3], the climate [4,5], and human health (e.g., because of intoxication due to SO_2, which can be inhaled by people living near active volcanic areas) [6,7]. Furthermore, SO_2 can serve as a proxy for volcanic ash plumes [8,9], which pose a significant threat to aircraft engines [10]. Additionally, it can be used to assess the state of a volcano and the progression of an individual eruption. Finally, temporal variations in SO_2 flux can indicate impending volcanic eruptions [11]. Therefore, improving the quality, frequency, and timeliness of volcanic SO_2 measurements is of great interest to the scientific community and may provide more information to expert users and decision-makers. SO_2 is also more easily detected and measured than ash, although it poses a lower threat to jet aircrafts. In scenarios where ash and SO_2 are expected to coexist and move together, a logical strategy is to identify SO_2 and use it as a proxy to determine the airspace that is potentially affected by ash.

Satellite-based remote sensing represents a unique and valuable technology for monitoring volcanic emissions globally, being the most cost-effective and accessible means for global volcanic cloud monitoring [12]. In fact, this is the only means of monitoring emissions from the most remote regions on Earth, which are sparsely equipped with ground-based and in situ systems. In addition, thanks to its synoptic view, satellite technology is often the only way to monitor large-scale phenomena such as volcanic emissions in the atmosphere, which may travel for hundreds or thousands of kilometers from the source in a relatively short time and persist aloft for extended periods [12].

Currently, a variety of geostationary (GEO) multispectral satellite sensors with bands in the thermal infrared (TIR) region are used for the identification, near-real-time monitoring, and retrieval of volcanic SO_2. The SEVIRI [13,14] and the Advanced Himawari Imager (AHI) [15,16] are two sensors operating onboard the European Meteosat Second-Generation (MSG) and Japanese HIMAWARI platforms, respectively. TIR instruments aboard polar-orbiting satellites have also been employed, such as multispectral scanners, including the Advanced Spaceborne Thermal Emission and Reflection Radiometer (ASTER) [17], Moderate-Resolution Imaging Spectroradiometer (MODIS) [13,18], and Visible Infrared Imaging Radiometer Suite (VIIRS) [19], and sounding spectrometers, including the Infrared Atmospheric Sounder Interferometer (IASI) [20] and the Atmospheric Infrared Sounder (AIRS) [21,22]. In addition, other instruments that do not operate in the TIR region have significantly advanced the detection of previously undetectable SO_2 emissions because of their high sensitivity and/or spatial resolution, such as the Total Ozone Mapping Spectrometer (TOMS) [23], Global Ozone Monitoring Experiment-2 (GOME-2) [24], the Scanning Imaging Absorption Spectrometer for Atmospheric Cartography (SCIAMACHY) [25], the Ozone Monitoring Instrument (OMI) [26], and, more recently, TROPOMI [13,15]. Although these sensors on low-Earth-orbit (LEO) platforms provide valuable data, their long revisit times and the capacity for detection only during daylight hours limit their ability to capture

rapid changes in SO_2 emissions, as highlighted by previous studies [22]. On the other hand, near-real-time monitoring is critical for early warning systems and continuous tracking of volcanic plumes, which is a key aspect of aviation safety, air quality management, and hazard mitigation [27,28]. High-frequency monitoring relies heavily on the high temporal resolution that only geostationary systems can provide, ensuring timely detection and near-continuous responses to evolving threats [12].

It is well documented in the literature that the 8.7 μm band on SEVIRI is particularly effective for volcanic SO_2 detection because of its strong and characteristic absorption feature, which enables the sensitive identification of SO_2 plumes with less interference from atmospheric water vapor when compared with the 7.3 μm band, which suffers from greater water vapor absorption [22,29–31]. When combined with reference infrared channels, such as the 10.8 μm band, it can discriminate between SO_2 and volcanic ash [31]. Over the past few decades, volcanic SO_2 detection using infrared (IR) satellite data has evolved from simple threshold and band-difference techniques exploiting absorption features near 7.3 μm and 8.7 μm [23,29,31] to more advanced statistical, contextual, and multi-band methods that better account for atmospheric variability and reduce false positives [13,30]. The introduction of RGB composite products combining multiple IR channels, including SO_2 -sensitive and reference bands like 10.8 μm, has enabled intuitive and rapid plume visualization using geostationary sensors such as the SEVIRI and the AHI, which are widely adopted in operational volcanic monitoring [32]. More recently, machine learning techniques, including support vector machines and deep learning models, have demonstrated improved sensitivity and automation for SO_2 plume detection in IR imagery by leveraging large training datasets and complex pattern recognition [33–35].

Among the most recent methods developed to detect volcanic SO_2 plumes by exploiting the high temporal resolution of SEVIRI data, Robust Satellite Techniques (RSTs), a multi-temporal approach (Section 2.3), was preliminarily tested with success in a previous study [36] by investigating the Mt. Etna (Italy) eruption of December 2015. This method, which does not use fixed threshold tests and is based only on satellite observations, without requiring any ancillary data, may guarantee the effective identification of SO_2-affected areas under different observational conditions. This potential is more deeply assessed in this work, where the method was used for the first time to analyze the volcanic plume emitted during the long-lasting La Palma Tajogaite eruption.

To assess the accuracy of volcanic SO_2 detection, we compared the results retrieved from infrared SEVIRI data with those from some independent satellite-based products. In particular, the well-known EUMETSAT SEVIRI-based Ash RGB product [32] and the TROPOMI SO2CBR [37] were used to assess the RST detections. The Ash RGB product, which is based on SEVIRI data, was used here for a quantitative assessment of RST-SO_2 performance, while the TROPOMI-based product specifically developed for SO_2 retrieval (i.e., SP5 COBRA), at different spatial and temporal resolutions, was used for further comparison.

The aim of this work was to evaluate the contribution of the RST method to the near-real-time (NRT) detection and tracking of volcanic SO_2, as a complement to operational satellite-based products, which are generally very sensitive to low gas concentrations [37] but less resolved in the time domain [12].

2. Materials and Methods

2.1. Study Area

La Palma, among the Canary Islands, has the highest eruption frequency in historical times, with recorded eruptions dating back to 1585 [31]. The most recent Tajogaite eruption occurred in 2021 in the Cumbre Vieja rift zone. This area is the most active volcanic

system on La Palma, characterized by frequent fissure eruptions involving multiple vents aligned along kilometers-long fractures, producing silica-undersaturated basanite and alkali basalts [33,38,39].

The 2021 Tajogaite eruption started on 19 September at 14:00 local time (LT) in the Cabeza de Vaca area, on the western side of the Cumbre Vieja ridge (Figure 1a), and lasted 85 days [40,41] (Figure 1b,c). The eruption, which involved effusive and explosive activity from multiple vents distributed along a 500-meter-long NE–SW fissure [40], represents an example of a cone-forming, long-lasting hybrid eruption associated with a decoupled magma–gas system [42].

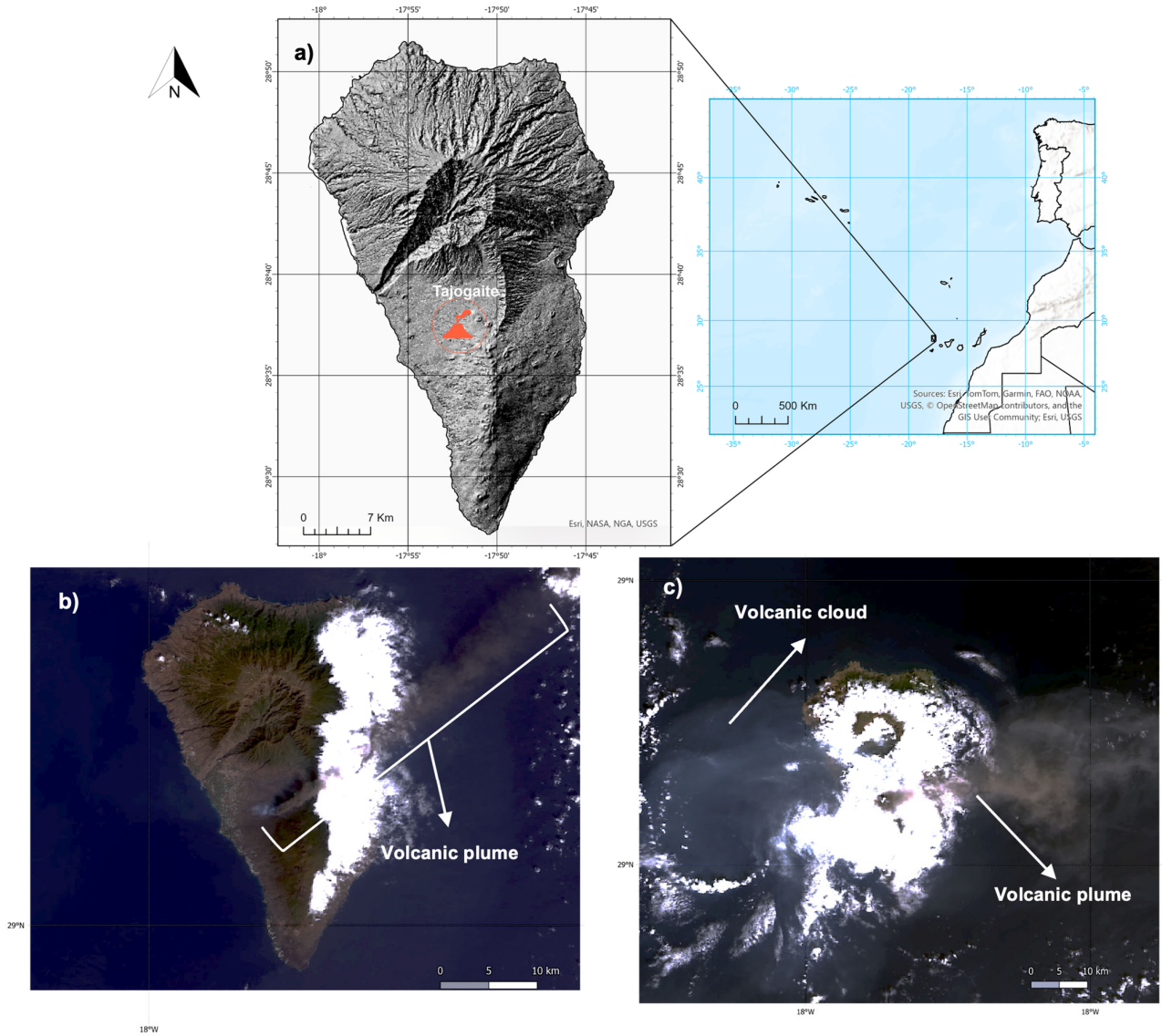

Figure 1. Study area. (**a**) Geographic location of the Tajogaite volcano on La Palma island; (**b**) Landsat 8 True Color image (Red = B04; Green = B03; Blue = B02) of 26 September 2021 at 11:42 UTC; (**c**) Landsat 8 True Color image of 12 October 2021 at 11:42 UTC. Both images show the volcanic plume emitted during the 2021 eruption (see the plume dispersing in the NE and E directions, respectively).

Large amounts of SO_2 were emitted and detected as far as the Caribbean and Central Europe. The eruption was accompanied by diffuse emission of CO_2 associated with the 220 km^2 Cumbre Vieja volcanic ridge [43]. The most recent estimate of the total SO_2

emission from the eruption was 1.6 (±0.1) Mt, with an upper limit of 1.9 Mt from a TROPOMI-derived estimate performed using PlumeTraj [44].

2.2. Data

2.2.1. MSG-SEVIRI

The SEVIRI sensor is aboard the MSG satellite platform. The instrument has twelve spectral channels, from visible to thermal infrared, and acquires full-disk data every 15 min (Figure 2). Eleven of its channels were acquired at a spatial sampling distance of 3 km at the nadir, and the high-resolution visible (HRV) channel was acquired at 1 km. Currently, SEVIRI flies on two main MSG platforms [45]: the Prime service (currently provided by the Meteosat-10 satellite), which scans the full disk, including Europe, the Atlantic Ocean, Africa, and locations where the elevation to the satellite is greater than or equal to 10°; and the Indian Ocean Data Coverage (IODC) service (presently provided by Meteosat-9). A third platform (Meteosat-11) also houses the SEVIRI sensor but for the rapid scanning service, which scans one-third of the Meteosat full disk every five minutes.

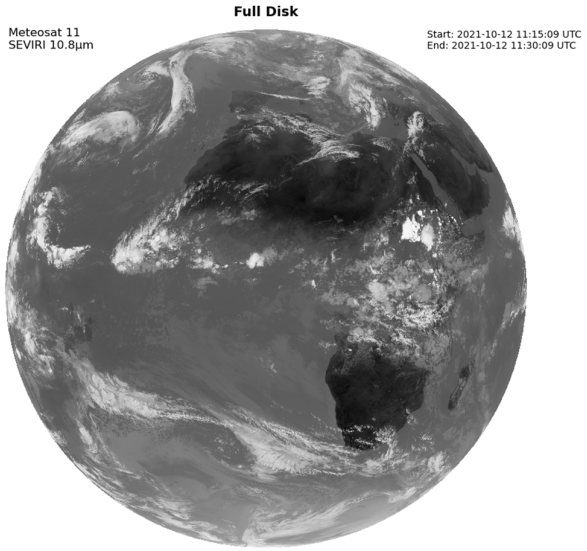

Figure 2. Full-disk thermal infrared (TIR) image from the SEVIRI at a 10.8 µm wavelength was acquired at 11:15 UTC on 12 October 2021.

We analyzed a time series of MSG-SEVIRI data acquired at the EUMETCast receiving station of the University of Basilicata (UNIBAS) in September and October at different time slots (i.e., 10:00, 12:00, 14:00, and 16:00 UTC) from 2007 to 2022. We extracted and used a selection of spectral channels (channel 1 (0.6 µm), channel 4 (3.9 µm), channel 7 (8.7 µm), channel 9 (10.8 µm), and channel 10 (12.0 µm)). Channels 1 and 9 were used to detect (and then exclude) cloudy radiances, a combination of channels 4, 7, and 9 was used to detect volcanic SO_2 plumes by optimizing the RST configuration first used in [29], and a combination of channels 7, 9, and 10 was used for the Ash RGB [32].

2.2.2. S5P Product Algorithm Laboratory (S5P-PAL)–L3 Grid Daily SO2CBR

In this work, we analyzed the Sentinel-5P TROPOMI SO_2 vertical column density product obtained using the COvariance-Based Retrieval Algorithm (COBRA), which was developed for the improved monitoring of the daily spatial and temporal distribution of this trace gas in the Earth's atmosphere globally [37]. This product, which merges all daily data retrieved in a grid file, is available at [46].

TROPOMI is a hyperspectral sensor aboard the Sentinel-5 Precursor (S5P) polar-orbiting satellite with a high spatial resolution of 3.5 × 7 km^2. It is a nadir-viewing, imaging spectrometer covering wavelength bands between the ultraviolet and the shortwave infrared, with daily global coverage in daylight [47].

2.3. Methodology

In this work, we investigated the SO_2 emissions from the Tajogaite eruption over the period 19 September–31 October 2021 using a specific configuration of the RST algorithm, exploiting SEVIRI channel 7 (centered at 8.7 μm), where a well-known SO_2 absorption band is present (see the Introduction section). Here, we focused on 43 days of the eruption, which had a long time duration (85 days), by analyzing infrared SEVIRI data acquired in four different time slots in daytime conditions.

2.3.1. The RST-Based Approach for SO_2 Plume Detection

The Robust Satellite Technique (RST) [48,49] is a multi-temporal approach to satellite data analysis that uses the Absolutely Local Index of Change of the Environment (ALICE) to detect anomalous variations in the signal ascribable to perturbing events:

$$\bigotimes_{V}(x,y,t) = \frac{V(x,y,t) - \mu_V(x,y)}{\sigma_V(x,y)} \quad (1)$$

where $V(x,y,t)$ is the signal value measured at time t and place (x,y). $\mu_V(x,y)$ and $\sigma_V(x,y)$ are the temporal mean and standard deviation, respectively; they represent the expected value and normal variability of the signal $V(x,y,t)$ itself. Here, we refer to these as "reference fields". The latter are computed by using a multi-year time series of homogeneous (e.g., same time of day, period of year) cloud-free satellite records.

The RST approach has been extensively used to detect and monitor volcanic hotspots (RST_{VOLC}, e.g., [50]) and ash plumes (RST_{ASH}, e.g., [51,52]) over several active volcanic areas, such as Mt. Etna [36,52,53], Agung (Indonesia) [54], Eyjafjallajokull (Iceland) [55], and Shinmoedake (Japan) [56].

Data from polar (e.g., AVHRR [36,51] and MODIS [57]) and geostationary (e.g., SEVIRI/AHI [36,54,55,58]) satellite sensors were used for this purpose, with some limitations discussed in detail in several previous papers (e.g., [50–56]). A detailed description of the RST approach for detection of volcanic ash/SO_2 can be found in previous studies [36,51–56].

To identify and track volcanic SO_2 plumes, a specific RST configuration was proposed in [36], exploiting the peculiar absorption characteristics of SO_2 in specific spectral regions [12,29,36,37] and the SEVIRI bands suited to distinguish ash from meteorological clouds (e.g., [59,60]):

$$\bigotimes_{BT8.7-BT10.8}(x,y,t) = \frac{(BT_{8.7}(x,y,t) - BT_{10.8}(x,y,t)) - \mu_{BT8.7-BT10.8}(x,y)}{\sigma_{BT8.7-BT10.8}(x,y)} \quad (2)$$

$$\bigotimes_{BT3.9-BT10.8}(x,y,t) = \frac{(BT_{3.9}(x,y,t) - BT_{10.8}(x,y,t)) - \mu_{BT3.9-BT10.8}(x,y)}{\sigma_{BT3.9-BT10.8}(x,y)} \quad (3)$$

where $V(x,y,t)$ in Equation (1) is equal to $BT_{8.7}(x,y,t) - BT_{10.8}(x,y,t)$ (i.e., the difference between brightness temperatures measured at 8.7 μm (SO_2 absorbing band) and 10.8 μm) and $BT_{3.9}(x,y,t) - BT_{10.8}(x,y,t)$ is the brightness temperature difference in the MIR and TIR bands. The other terms in Equations (2) and (3) have the same meaning as in Equation (1).

In the presence of a volcanic SO_2 plume, negative values of the $\bigotimes_{BT8.7-BT10.8}(x,y,t)$ index are expected due to different absorption features, while positive values of the $\bigotimes_{BT3.9-BT10.8}(x,y,t)$ index, when used in combination with the former index, should

reduce the occurrence of false detections in the daytime conditions investigated in this work [36].

2.3.2. Method Implementation

Starting from the SEVIRI full-disk imagery, we extracted a region of interest centered over La Palma island (see Figure 3 and the following). Infrared data (i.e., channel 4 (3.9 μm), channel 7 (8.7 μm), and channel 9 (10.8 μm)) were calibrated in brightness temperature [K], while the visible ones (channel 1) were calibrated in radiance (mW/m^2 sr cm^{-1}).

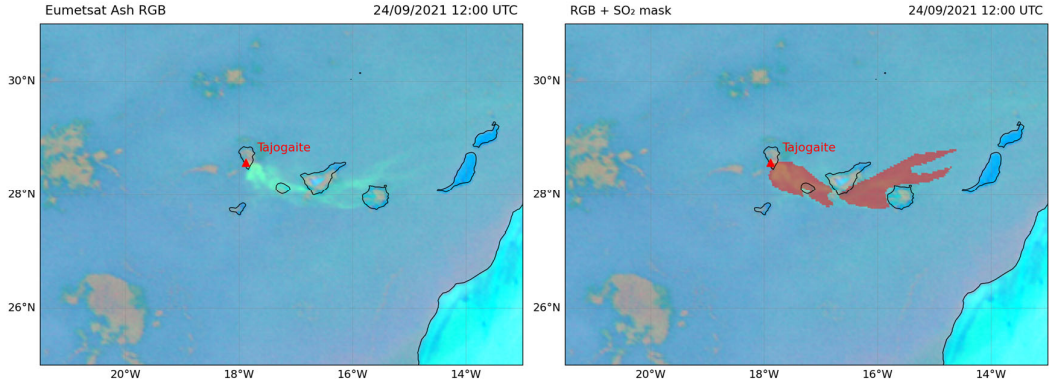

Figure 3. Left panel: EUMETSAT Ash RGB configuration of 24 September 2021 at 12:00 UTC showing, in bright green, SO_2 emissions from the Tajogaite eruption. Right panel: Ash RGB with the SO_2-drawn mask (semi-transparent red color) from the visual inspection used for validation. The mask was manually drawn using ArcGIS Pro (version 3.5.2). SO_2 was identified based on its appearance in the RGB composite, where it presented a characteristic greenish coloration.

Following the RST rules, we generated a multi-year (2007–2022) dataset of satellite observations on a monthly basis (September and October) for each considered time slot (10:00 UTC, 12:00 UTC, 14:00 UTC, and 16:00 UTC). More than 300 satellite records were used for each dataset, which is significantly higher than the minimum number (at least 80 images) required to generate reliable spectral reference fields [61]. These datasets were processed to generate the spectral reference fields, i.e., $\mu_{SO2\text{-}TIR}(x,y)$, $\sigma_{SO2\text{-}TIR}(x,y)$, $\mu_{MIR\text{-}TIR}(x,y)$, and $\sigma_{MIR\text{-}TIR}(x,y)$, which are required to compute the local variation indices described by Equations (2) and (3). During the computation, we filtered out the cloudy radiance pixels using the One-channel Cloudy-radiance-detection Approach (OCA, [62]), which was applied to the visible (0.6 μm) and infrared (10.8 μm) bands. Hence, only cloud-free pixels were analyzed in the following processing steps. To detect the SO_2 plumes, both indices in Equations (2) and (3) were computed for all the images acquired in September and October 2021. In more detail, the following RST configuration tailored to SO_2 detection was used:

$$\bigotimes_{BT8.7-BT10.8}(x,y,t) < -3 \text{ AND } \bigotimes_{BT3.9-BT10.8}(x,y,t) > 0 \quad (4)$$

$$\bigotimes_{BT8.7-BT10.8}(x,y,t) < -2 \text{ AND } \bigotimes_{BT3.9-BT10.8}(x,y,t) > 0 \quad (5)$$

This configuration was implemented to detect different SO_2 plume regions through an RST high confidence level (statistically more likely identification; Equation (4)) and an RST low confidence level (mapping larger plume portions with a possible accuracy reduction; Equation (5)).

2.3.3. Validation Method

To assess the RST detections, we compared them with masks drawn from the EUMETSAT Ash RGB configuration [32] (Figure 3) generated from the same sensor (SEVIRI) and, therefore, with the same spatial and temporal resolutions.

The Ash RGB product combines the brightness temperature (BT) of three SEVIRI TIR channels (Red: $BT_{12.0}-BT_{10.8}$; Green: $BT_{10.8}-BT_{8.7}$; Blue: $BT_{10.8}$ [32]). The channel combination in the red band is the reverse of the "split window" method [59]; thin volcanic ash tends to have a strong reddish color, whereas meteorological clouds do not contribute. The green band channel shows the presence of SO_2, comparing the SO_2 absorption band at 8.7 μm with the non-absorbing 10.8 μm band. Finally, the 10.8 μm in the blue band provides a high-contrast background for ash detection and removes the influence of cumulonimbus clouds. Depending on the concentration, the red pixels indicate the presence of thin volcanic ash, green pixels indicate the presence of SO_2, and yellow pixels indicate mixed regions of a volcanic cloud containing both ash and SO_2. The Ash RGB imagery is subject to certain constraints, particularly in the accurate identification of ash and SO_2 when these elements are combined with cirrus or ice clouds [33]. Furthermore, a notable constraint is the viewing angle, as the color representation in SEVIRI Ash RGB images is contingent upon this factor. When the satellite viewing angle exceeds 65 degrees, distinguishing the components of the volcanic cloud, especially SO_2, becomes challenging. This difficulty arises because water clouds manifest a green color that closely resembles that of SO_2. When the satellite viewing angle was close to the sub-satellite point, the volcanic cloud components could be discriminated more easily and accurately than at other angles. However, the main advantage of using this type of image is the ease of recognition of the different components of the volcanic cloud owing to its intuitive colors [33]. The pixels of the Ash RGB image were normalized between 0 and 1.

Using the mask as a base, we performed an evaluation using a confusion matrix [61], because our output was a binary classification mask. It compares the RST-predicted classifications against the masks obtained from the labeled ash RGB, identifying the following possible outcomes:

- True Positive (TP): The number of pixels where SO_2 was correctly detected.
- False Positive (FP): The number of pixels where SO_2 was incorrectly detected.
- True Negative (TN): The number of pixels correctly identified as not containing SO_2.
- False Negative (FN): The number of pixels where SO_2 was missed.

These outcomes allowed us to compute the following performance metrics.

- Accuracy is the proportion of correctly classified pixels, both positive and negative, relative to all evaluated pixels.

$$\frac{TP + TN}{TP + FP + TN + FN} \tag{6}$$

- Precision, that is, the proportion of SO_2 detections that are correct.

$$\frac{TP}{TP + FP} \tag{7}$$

- Recall (or sensitivity), that is, the ability of the method to detect all actual SO_2 pixels.

$$\frac{TP}{TP + FN} \tag{8}$$

- F1-Score, representing the harmonic mean of precision and recall. It provides a single measure that balances both false positives and false negatives, which is especially useful when data are imbalanced.

$$2 \times \frac{(\text{Precision} \times \text{Recall})}{\text{Precision} + \text{Recall}} = \frac{2 \times \text{TP}}{2 \times \text{TP} + \text{FP} + \text{FN}} \quad (9)$$

- The false-positive rate (FP rate) is the proportion of actual negatives incorrectly predicted as positive.

$$\frac{\text{FP}}{\text{FP} + \text{TN}} \quad (10)$$

To evaluate the method's performance across multiple days and images, we applied three precision, recall, and F1-score averaging strategies [63]:

- Micro average: This aggregates the total TP, FP, and FN across all detections and computes the metric globally.
- Macro average: Computes the metrics for each image individually and averages them equally.
- Weighted average: Computes the metrics per image but weights them according to the number of pixels in each sample.

In instances where the reference data lacked SO_2 (i.e., no true positives or false negatives), the recall and F1-score were undefined and consequently omitted from the average calculations. This approach prevents skewing of the overall evaluation due to the absence of detectable events. This evaluation ensured a comprehensive and interpretable assessment of the detection performance across varying plume intensities, background conditions, and detection thresholds.

3. Results

To evaluate the performance of the RST-SO_2 algorithm, a comprehensive validation was conducted using 168 SEVIRI images collected over 43 days during the September–October 2021 eruptive phase of the Tajogaite volcano. The validation employed manually drawn reference masks based on visual inspection of the areas affected by the sulfur dioxide in the EUMETSAT Ash RGB composite. The masks were used to determine the presence or absence of volcanic SO_2 clouds in each image.

Detection of SO_2 was defined as any time step where the reference dataset indicated the presence of SO_2 (i.e., true positives > 0), being able to detect SO_2 on 81.40% of the eruption days. Conversely, on 18.60% of the days, no SO_2 was detected in any of the evaluated time slots (10:00, 12:00, 14:00, or 16:00 UTC). Specifically, SO_2 was absent on 8 days, and 5 days also were not detected in the RGB composite (Table 1).

Table 1. Comparison between the RST-SO_2 configuration using two confidence levels (second and third columns) and the Ash RGB product (fourth column). Days with no detection are marked by "-", while days with SO_2 detection are indicated by "X". The last column reports the daily SO_2 estimations from Esse et al. [44]. The supporting material contains information for all days.

Date	RST High Confidence	RST Low Confidence	Ash RGB	SO2 Emission (kt/day)
22/09/2021	-	X	X	~60
27/09/2021	-	-	-	~9
08/10/2021	-	-	-	~38
14/10/2021	-	-	X	~10
19/10/2021	-	-	-	~17
22/10/2021	-	-	X	~28
23/10/2021	-	-	-	~9
27/10/2021	-	-	-	~13

Table 1. *Cont.*

Date	RST High Confidence	RST Low Confidence	Ash RGB	SO2 Emission (kt/day)
28/10/2021	-	X	X	~15
31/10/2021	-	-	X	~15

Table 1 presents a comparison of the daily SO_2 emission estimates from Esse et al. [44] with RGB-based detection. This comparison confirmed that some detections were missed when the estimated SO_2 mass was low (<15 kt/day), thereby supporting the hypothesis of weak or obscured plumes.

The pixel-based confusion matrices presented in Figure 4 demonstrate a high level of agreement with the reference data. For the low-confidence product, TPs accounted for 0.6% of the total pixels, FPs represented 2.0%, TNs were predominant at 97.0%, and FNs accounted for 0.4%, being less restrictive having fewer TNs. In contrast, the high-confidence product exhibited a reduced FP rate of 0.3%, a slightly lower TP rate of 0.5%, a significantly higher TN rate of 98.7%, and an FN rate of 0.5%, being more restrictive having more TNs. Hence, the high-confidence product provided a more conservative classification, prioritizing specificity over sensitivity.

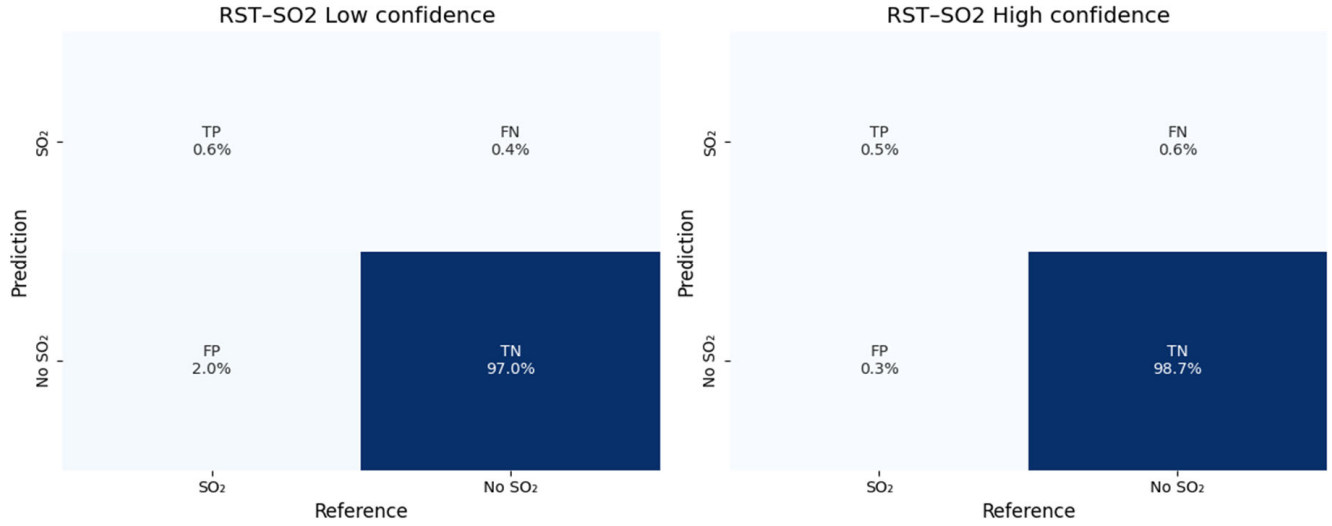

Figure 4. Confusion matrix for low-and high-confidence products.

The confusion matrix (Figure 4) shows a class imbalance where the TN rate (background "No SO_2") is 97% (low-confidence level) to 99% (high-confidence level) of the pixels, dominating the class and making overall accuracy uninformative. To address this issue and obtain a more informative evaluation, we conducted a performance evaluation considering precision, F1-score, and recall. To summarize performance fairly, we report micro, macro, and weighted averages (Figure 5).

In the analysis of the macro and weighted averages, the more restrictive product demonstrated superior precision (~79%) and a higher F1-score (~54.6%), although its recall was lower than that of the low-confidence RST-SO_2 product (Figure 5). This observation underscores the trade-off between detection sensitivity and over-detection. The low-confidence approach prioritizes recall (minimizing missed detections), whereas the high-confidence approach emphasizes higher confidence in detection.

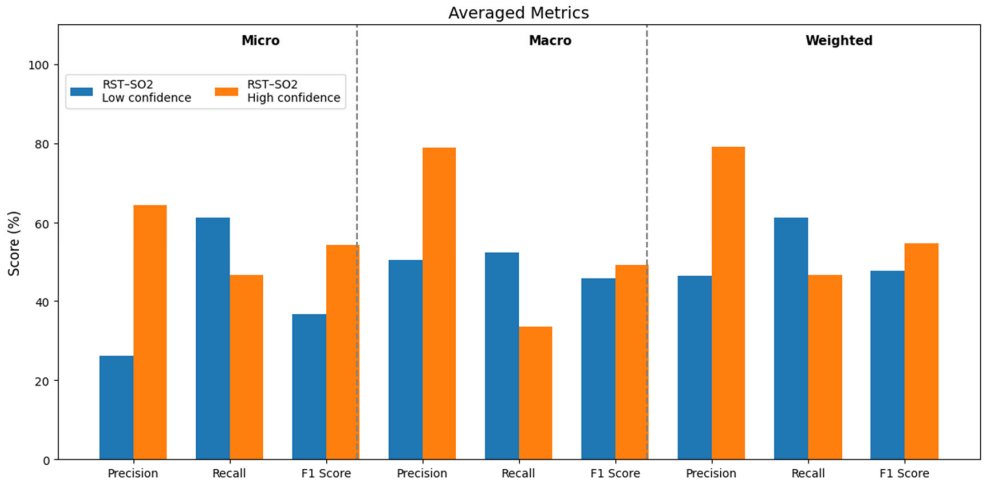

Figure 5. Results of the averaging metric comparison.

To further understand the practical capabilities of the algorithm, we identified four good-performing days based on the average F1-score across both products (Figure 6). These days reflect cases where both RST-SO_2-based products achieved high precision and recall, suggesting robust detection across confidence levels. These examples highlight the capacity of the RST-SO_2 approach to achieve excellent performance under favorable plume and atmospheric conditions. It is also possible to verify that the RST approach was able to detect emissions as low as 10 kt/day [44] on 29 October at 14:00 UTC, as well as the plume direction and dispersion.

An examination of the daily false-positive rates identified significant increases coinciding with dust outbreaks, particularly during the periods of 25 September–4 October and 16–22 October (Figure 7). These dates were also associated with elevated aerosol optical depth (AOD) values, indicating that Saharan dust may have contributed to spectral confusion. This was especially evident for the less restrictive product, which exhibited a temporary increase in false-positive rates of up to 30% during these events. In Figure 6c, false positives affecting the southwestern part of the analyzed area (yellow pixels) were probably caused by meteorological clouds.

Comparison Between S5P-PAL SO_2 and RST-SO_2 Products

To further assess the quality of the RST-SO_2 product, we performed a systematic comparison with the TROPOMI-based product by analyzing the SEVIRI data closest to the selected time slots analyzed in the study (i.e., 14:00 UTC). The SO_2 mask from S5P-PAL was obtained by extracting only pixels with values different from zero of this TROPOMI product for the same domain as the RST-SO_2 product. On 23 September (Figure 8a), the RST detected the SO_2 plume northeast of La Palma, which closely coincided with the highest SO_2 columns retrieved by TROPOMI. On 24 September (Figure 8b), RST-SEVIRI detections at a high confidence level were still consistent with the information provided by TROPOMI, although the latter captured a broader lower concentration around the main cloud. On 25 September (Figure 8c), the RST-SEVIRI detections matched with the central part of the TROPOMI plume. However, unlike TROPOMI, no information was provided regarding the distal region of the plume. Indeed, as for 29 September (Figure 8d), the RST-SEVIRI product highlighted the densest zones near and downwind of the volcano, while TROPOMI delineated the full spatial extent of the plume at lower SO_2 concentrations. The general good agreement between the two different satellite-based products characterized other satellite observations of September 2021 (except for 22 and 27 September; see the Supplementary Materials), although TROPOMI enabled a more accurate and complete identification of volcanic SO_2.

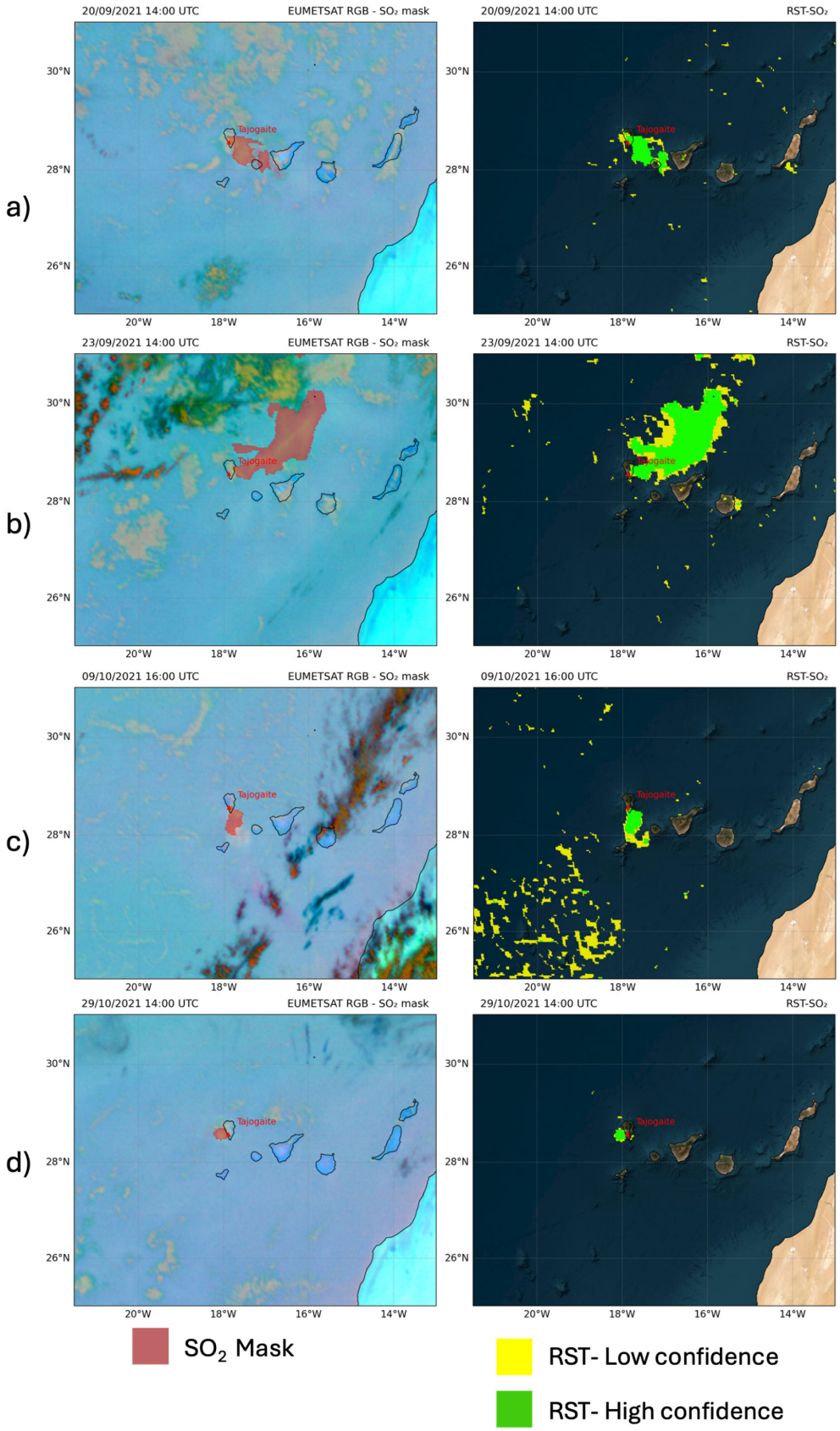

Figure 6. RST-based SO_2 maps from MSG/SEVIRI data. In yellow, the low-detection-confidence product ($\otimes_{SO2\text{-}TIR}(x,y,t) < -2$ AND $\otimes_{MIR\text{-}TIR}(x,y,t) > 0$); in bright green, the high-confidence-level product ($\otimes_{SO2\text{-}TIR}(x,y,t) < -3$ AND $\otimes_{MIR\text{-}TIR}(x,y,t) > 0$). The red marker is the volcano location.

(**a**) RST-based SO_2 map for 09/10/2021 with an average F1-score of 0.70, (**b**) RST-based SO_2 map for 23/09/2021 with an average F1-score of 0.84, (**c**) RST-based SO_2 map for 20/09/2021 with an average F1-score of 0.73, and (**d**) RST-based SO_2 map for 29/10/2021 with an average F1-score of 0.61.

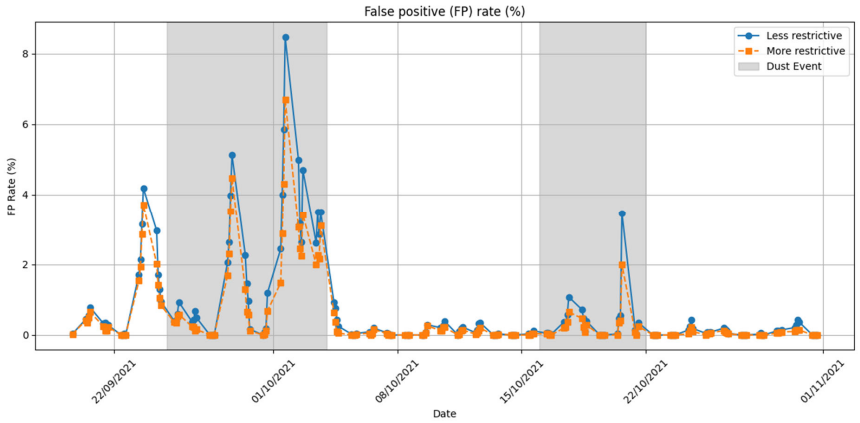

Figure 7. False-positive rate of the RST-based product compared with the Ash RGB mask. Days notoriously affected by a dust storm [64] are reported as well.

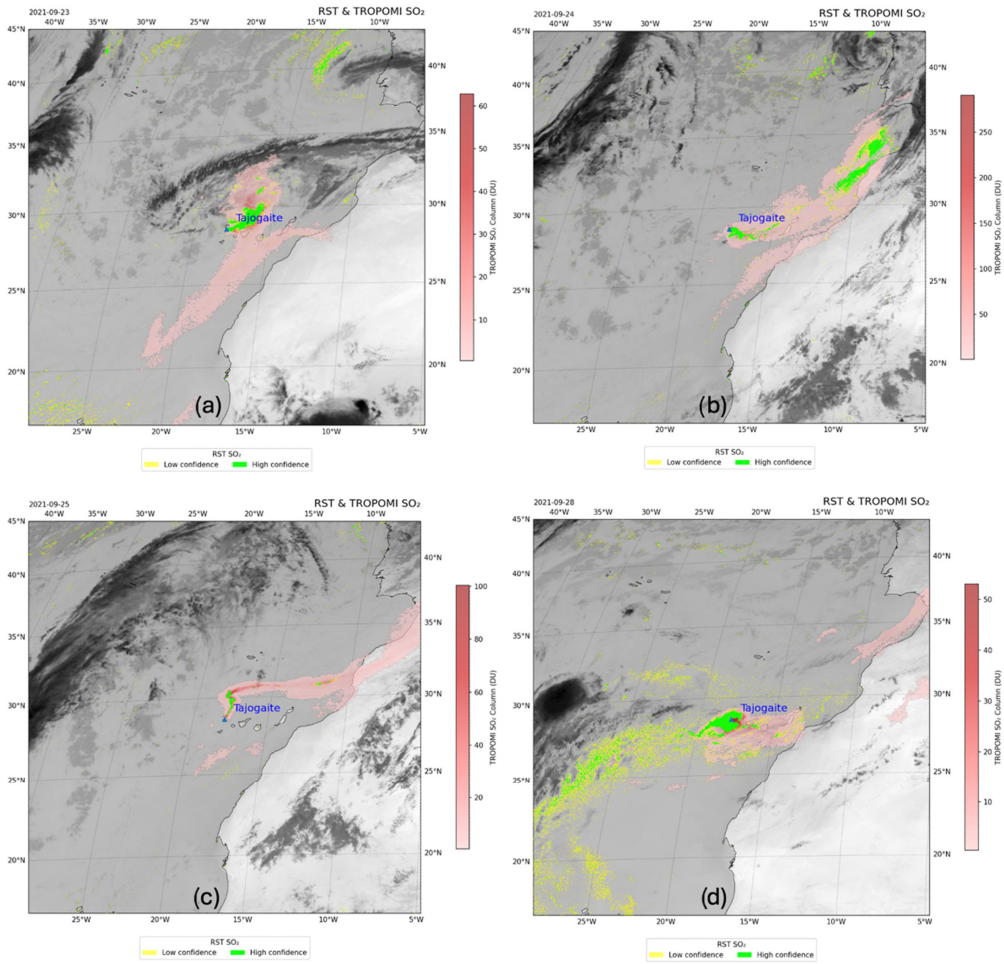

Figure 8. SO_2 detection comparison between the S5P-PAL product from the TROPOMI acquisition on days 23 (**a**), 24 (**b**), 25 (**c**), and 29 (**d**) of September 2021 around 14:00 UTC (color bar indicates an SO_2 column, more intense red indicates a higher SO_2 column, and white indicates no SO_2), and the RST-SO_2 product from SEVIRI data of the same day at 14:00 UTC. TROPOMI detections are overlapped on the SEVIRI 10.8 µm channel (band 9), image shown in the background.

Figure 9 shows the results of the comparison for October 2021. On 1 October (Figure 9a), RST-SEVIRI detections matched information from TROPOMI. In more detail, the latter outlined a broader envelope extending further from the source, while the volcanic plume was detected by the RST method through SEVIRI data, where the higher SO_2 column value was, as for 2 October (Figure 9b). On 3 October (Figure 9c), both satellite products still provided similar information about plume shape and direction. On the other hand, TROPOMI resolved the full spatial footprint, including diffuse areas extending beyond SEVIRI's detection limits as for 20 October (Figure 9c).

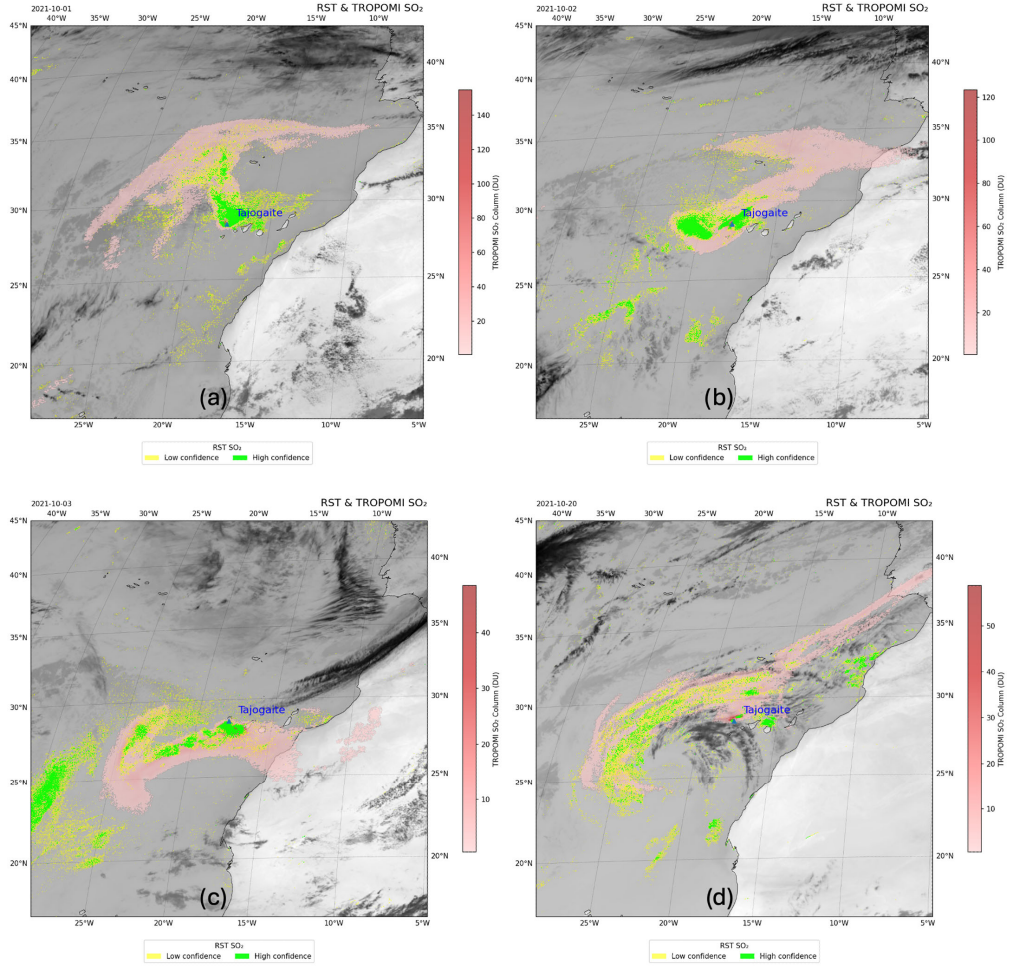

Figure 9. SO_2 detection comparison between the S5P-PAL product from the TROPOMI acquisition of days 1 (**a**), 2 (**b**), 3 (**c**), and 20 (**d**) of October 2021 around 14:00 UTC (color bar indicates an SO_2 column, more intense red indicates a higher SO_2 column, and white no SO_2), and the RST-SO_2 product from SEVIRI data of the same day at 14:00 UTC. TROPOMI detections are overlapped on the SEVIRI 10.8 µm channel (band 9), image shown in background.

The consistent spatial correspondence between the RST-SEVIRI product and the information provided by TROPOMI across all images (Figures 8 and 9), especially in regions with higher SO_2 concentrations, highlights the effectiveness of the method in a possible operational context.

Hence, the RST-SEVIRI product detected the plume regions at a higher SO_2 concentration, while it was generally less effective at higher distances from the source, although in some cases it provided information about the distal regions of the plume, unlike the Ash RGB product, despite some limitations. For instance, Figure 10 shows that the SO_2 plume detected by TROPOMI on 23 October 2021 at 13:52 UTC was partially detected by the RST

method using SEVIRI data closest in time (14:00 UTC). The analysis of the SO_2 product from the Atmospheric Infrared Sounder (AIRS) of the Support to Aviation Control Service (SACS) [65] (Figure 10b) did not reveal, however, any presence of volcanic SO_2 over that region, indicating that a reduction in sensitivity may affect infrared satellite observations.

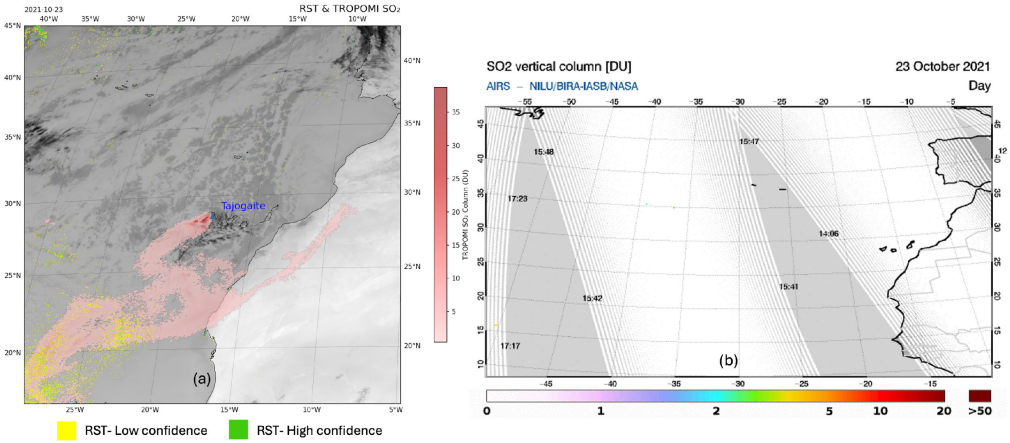

Figure 10. (**a**) SO_2 detection comparison between the S5P-PAL product from the TROPOMI acquisition on 23 October 2021 at 13:52 UTC with overlap of the RST-SO_2 product from MSG/SEVIRI data of the same day at 14:00 UTC (TROPOMI detections are overlapped on the SEVIRI 10.8 μm channel (band 9), image shown in background) and (**b**) the SACS AIRS SO_2 product on the same day at 14:06 UTC.

It is worth noting that comparison with the S5P-PAL product allowed us to infer information about the dependence of the method used on plume intensity and/or dispersion/dilution. Although a separate analysis was performed for the two confidence levels, findings regarding the relationship with DUs were quite similar for both RST-SEVIRI detection products (over all 43 days analyzed, the minimum DU detected was found to be equal to 0.43 and the maximum was 740.62). In general, the RST method detected the volcanic SO_2 in the proximity of the source, even if the higher sensitivity of the mid/low-confidence product enabled a more efficient detection at longer distances, up to approximately 1850 km from the volcano, against ~1700 km of the high-confidence-level product.

It is worth mentioning that, owing to the sensor-dependent limitation, it was not possible to make a further quantitative comparison between the TROPOMI S5P-PAL and RST-SEVIRI products. Missed detections, ascribable to the different sensitivities of the two sensors, would have had a significant impact on the class of "false negatives" and the resulting metrics. However, a comparison between the two products was carried out to quantify the false-positive rate affecting RST-SO_2 detections. This metric was found to be very low, averaging 1.7% for the mid/low-confidence RST product and 0.3% for the high-confidence-level product, over all 43 days analyzed. As already shown, dust clouds were probably the main source of false detections, as the false-positive rate reached its highest value (7.5% for the low-level product, 1.8% for the high-level product) during or immediately after some documented Saharan dust events (see Figure 7). However, meteorological clouds also affected the SO_2 detection, especially since dense/opaque or ice clouds can mask the underlying volcanic SO_2. Overall, the high-confidence RST-SO_2 product is more conservative and specific (FP 0.3%, TN 98.7%), yielding higher precision (~79%) and a higher F1-score (~54.6%) but lower recall and TP (0.5%), guaranteeing reliable plume detection. The low-confidence product prioritizes sensitivity (TP 0.6%) and higher recall, detecting weaker and distal regions of the plumes at the expense of a higher FP, owing to cloud-related artefacts. Operationally, the two products are used jointly to enable more effective tracking of SO_2 plumes.

4. Discussion

The RST-SO_2 method applied to the SEVIRI data demonstrated strong potential for operational SO_2 detection, particularly when leveraging both low- and high-confidence outputs. Despite the inherent challenges in thermal SO_2 detection [30], this approach yielded a recall of over 60% for the low-confidence and more permissive product and a precision exceeding 64% for the high-confidence and more conservative product, achieving a practical balance between the sensitivity and reliability of the results.

These results are consistent with the results of previous applications of TIR-based SO_2 detection. For example, Corradini et al. [22,30] demonstrated the utility of the SEVIRI sensor for detecting volcanic SO_2 in the case of Mt. Etna eruptions, with variable success depending on emission strength and cloud coverage. Similarly, other studies [8,18] have shown that ash and dust aerosols interfere with SO_2 retrievals, particularly in the 8.7 µm spectral band of the SEVIRI.

The plume and its evolution were identified for 35 of the 43 days analyzed (Table 1), and, on five of the eight eruption days when the RST-SO_2 products did not provide any information, the SO_2 plume was not evident in the Ash RGB product. To better understand the possible causes of missing detection, we compared the TROPOMI product (operating in the UV spectral range) with the SO_2 product from SACS based on AIRS measurements in the infrared spectral range [64], both acquired over La Palma island at approximately 14:06 UTC (Figure 10b). Notably, the AIRS as well as SEVIRI failed to detect the SO_2 plume, despite its higher sensitivity in detecting this type of emission. This analysis suggests that the missed detections were likely due to spectral limitations, specifically the generally lower sensitivity of infrared sensors to weak SO_2 signals.

In more detail, the SO_2 retrieval in the 8.7 µm channel of the SEVIRI is sensitive to plume height, water vapor, ash concentration, and thermal contrast with the background [22,31,64]. Our analysis identified scattered false positives and missed detections during the monitoring period. Nonetheless, the false-positive rate remained notably low (2%) for the low-confidence RST product, and only 0.3% for the high-confidence product. In the proximity of the source, a significant impact of volcanic ash was observed, a phenomenon that has been well documented in previous studies [31,59,66]. This interference was particularly evident between 28 September and October 4, when the undetected portions of the volcanic plume coincided with a higher ash concentration. These findings are consistent with those of a previous study [44], which showed lower agreement between satellite and ground-based estimations in the presence of increased ash emissions.

An essential factor in assessing SO_2 detection is the inherent class imbalance present in satellite imagery, in which most pixels represent background conditions. This imbalance inflates the true negative counts and can distort the effectiveness of the accuracy as a performance metric. Consequently, the precision, recall, and F1-score, particularly their macro, micro, and weighted averages, are more appropriate for evaluating detection proficiency. In our findings, RST-SO_2 low-confidence detections achieved a higher recall (52.3% macro), indicating a preference for sensitivity, whereas RST-SO_2 high-confidence detections demonstrated higher precision (79.3% weighted).

The high temporal resolution of the SEVIRI (15 min intervals) represents a distinct strength over polar-orbiting platforms such as TROPOMI, despite the relevant information provided by this instrument (e.g., [67]). Indeed, although UV-based sensors are more sensitive to volcanic SO_2 [37,67], they are limited to daytime conditions, thereby limiting their utility for continuous monitoring [68], whereas the SEVIRI can be used for the near-real-time tracking of SO_2 dispersion [69].

The RST configuration used in this study relied solely on satellite records without requiring external data inputs, primarily serving as a detection method rather than a

quantitative retrieval procedure. Therefore, despite the limitations, especially in terms of sensitivity, affecting infrared SEVIRI observations, we found that RST detected SO_2 plume column densities as low as ~0.43 DU and successfully detected SO_2 on 35 eruption days when the low confidence level was used (i.e., an ~81% detection rate on a daily basis). The high-confidence detections revealed the volcanic plume on 33 eruption days, corresponding to an overall success rate of approximately 80%. Moreover, the high temporal resolution of the SEVIRI enabled accurate tracking of the plume and the presence of volcanic SO_2 on 81% of the eruption days [42,43,70].

5. Conclusions

In this study, we used the RST configuration tailored to volcanic SO_2 detection to monitor the SO_2 plume emitted during the 2021 Tajogaite eruption by analyzing infrared SEVIRI data from 19 September to 31 October.

This configuration was preliminarily tested in [36] by analyzing the Mt. Etna eruption of December 2015 in two specific time slots (i.e., 05:00 UTC and 08:00 UTC).

Here, we have extensively used this algorithm configuration over a two-month period across four daily time slots (10:00, 12:00, 14:00, and 16:00 UTC). The results were assessed by assessing RST detections by means of the well-established and widely used EUMETSAT Ash RGB product. Despite the impact of atmospheric constituents and sensor limitations on the identification of SO_2 plumes, the RST algorithm had an overall average precision of ~79% and an F1-score of 55%. Indeed, areas affected by SO_2 were generally well-identified in both the proximal and distal regions of the volcanic plumes. The sensitivity of the algorithm was quantified with an overall detection rate based on high-confidence detection matches of approximately 81%, confirming the robustness of the method, which can then be used for automated detection and tracking of volcanic SO_2 plumes. The RST configuration tested in this work could also be extensively used to detect volcanic SO_2 from other active volcanoes (e.g., Etna, Stromboli) covered by the SEVIRI.

Indeed, this instrument, by offering 96 observations per day in the full-disk configuration, may contribute significantly to the NRT monitoring of volcanic SO_2, which can be used as a proxy for volcanic ash and is particularly relevant for applications in hazard assessment and aviation safety.

The Flexible Combined Imager (FCI) aboard Meteosat Third-Generation (MTG) satellites, by providing full-disc imagery every 10 min with a spatial resolution of 2 km in the infrared bands [71], will further improve the capacity of detecting and tracking volcanic SO_2 in a continuous way from space.

Supplementary Materials: The following supporting information can be downloaded at: https://www.mdpi.com/article/10.3390/rs17193345/s1. Word document (table comparing RST detections with estimations of SO_2 emissions from other studies),and a excel file with an event resume (RST detections, VAAC and Smithsonian Reports, and PEVOLCA Reports), and all images produced for each day analyzed for the RST product, TROPOMI, and RST–TROPOMI comparison.

Author Contributions: R.M., C.F., V.T. and N.P. conceived the research work. R.M. and C.F. wrote the paper and python code to run and implement the RST algorithm on MSG/SEVIRI data. R.M. performed the tests. F.M., A.F., N.P., V.T., A.G. and J.P. contributed to reviewing and editing the paper. All authors have read and agreed to the published version of the manuscript.

Funding: Fundação para a Ciência e Tecnologia: https://doi.org/10.54499/UI/BD/153514/2022; Fundação para a Ciência e Tecnologia: UIDP/00643/2020, DOI: 10.54499/UIDP/00643/2023.

Data Availability Statement: S5P Product Algorithm Laboratory (S5P-PAL)–L3 grid Daily SO2CBR data are available at https://data-portal.s5p-pal.com/products/so2cbr.html, accessed on 16 September 2025.

Acknowledgments: The authors wish to thank EUMETSAT and the Aeronautica Militare Italiana for providing access to the MSG/SEVIRI data used in this work. We also want to thank the three anonymous reviewers for their comments and suggestions that helped to improve the quality of this work.

Conflicts of Interest: The authors declare no conflicts of interest.

References

1. Oppenheimer, C.; Scaillet, B.; Martin, R.S. Sulfur Degassing from Volcanoes: Source Conditions, Surveillance, Plume Chemistry and Earth System Impacts. *Rev. Mineral. Geochem.* **2011**, *73*, 363–421. [CrossRef]
2. Shinohara, H. Excess Degassing from Volcanoes and Its Role on Eruptive and Intrusive Activity. *Rev. Geophys.* **2008**, 46. [CrossRef]
3. Wilson, T.M.; Stewart, C.; Sword-Daniels, V.; Leonard, G.S.; Johnston, D.M.; Cole, J.W.; Wardman, J.; Wilson, G.; Barnard, S.T. Volcanic Ash Impacts on Critical Infrastructure. *Phys. Chem. Earth Parts A/B/C* **2012**, *45–46*, 5–23. [CrossRef]
4. Craig, H.; Wilson, T.; Stewart, C.; Outes, V.; Villarosa, G.; Baxter, P. Impacts to Agriculture and Critical Infrastructure in Argentina after Ashfall from the 2011 Eruption of the Cordón Caulle Volcanic Complex: An Assessment of Published Damage and Function Thresholds. *J. Appl. Volcanol.* **2016**, *5*, 7. [CrossRef]
5. Bourassa, A.; Robock, A.; Randel, W.J.; Deshler, T.; Rieger, L.; Lloyd, N.D.; Llewellyn, E.J.; Degenstein, D.A. Large Volcanic Aerosol Load in the Stratosphere Linked to Asian Monsoon Transport. *Science* **2012**, *337*, 78–81. [CrossRef]
6. Heaviside, C.; Witham, C.S.; Vardoulakis, S. Potential health impacts from sulphur dioxide and sulphate exposure in the UK resulting from an Icelandic effusive volcanic eruption. *Sci. Total Environ.* **2021**, *774*, 145549. [CrossRef]
7. Vita, F.; Schiavo, B.; Inguaggiato, C.; Cabassi, J.; Venturi, S.; Tassi, F.; Inguaggiato, S. Output of Volcanic SO_2 Gases and Their Dispersion in the Atmosphere: The Case of Vulcano Island, Aeolian Archipelago, Italy. *Atmosphere* **2025**, *16*, 651. [CrossRef]
8. Thomas, H.E.; Prata, A.J. Sulphur Dioxide as a Volcanic Ash Proxy during the April–May 2010 Eruption of Eyjafjallajökull Volcano, Iceland. *Atmos. Chem. Phys.* **2011**, *11*, 6871–6880. [CrossRef]
9. Sears, T.M.; Thomas, G.E.; Carboni, E.; A. Smith, A.J.; Grainger, R.G. SO2 as a Possible Proxy for Volcanic Ash in Aviation Hazard Avoidance. *J. Geophys. Res. Atmos.* **2013**, *118*, 5698–5709. [CrossRef]
10. Casadevall, T.J. The 1989–1990 Eruption of Redoubt Volcano, Alaska: Impacts on Aircraft Operations. *J. Volcanol. Geotherm. Res.* **1994**, *62*, 301–316. [CrossRef]
11. Olmos, R.; Barrancos, J.; Rivera, C.; Barahona, F.; López, D.L.; Henriquez, B.; Hernández, A.; Benitez, E.; Hernández, P.A.; Pérez, N.M.; et al. Anomalous Emissions of SO_2 during the Recent Eruption of Santa Ana Volcano, El Salvador, Central America. *Pure Appl. Geophys.* **2007**, *164*, 2489–2506. [CrossRef]
12. Mota, R.; Pacheco, J.M.; Pimentel, A.; Gil, A. Monitoring Volcanic Plumes and Clouds Using Remote Sensing: A Systematic Review. *Remote Sens.* **2024**, *16*, 1789. [CrossRef]
13. Corradini, S.; Guerrieri, L.; Stelitano, D.; Salerno, G.; Scollo, S.; Merucci, L.; Prestifilippo, M.; Musacchio, M.; Silvestri, M.; Lombardo, V.; et al. Near Real-Time Monitoring of the Christmas 2018 Etna Eruption Using SEVIRI and Products Validation. *Remote Sens.* **2020**, *12*, 1336. [CrossRef]
14. Gauthier, P.-J.; Sigmarsson, O.; Gouhier, M.; Haddadi, B.; Moune, S. Elevated Gas Flux and Trace Metal Degassing from the 2014–2015 Fissure Eruption at the Bárðarbunga Volcanic System, Iceland. *J. Geophys. Res. Solid Earth* **2016**, *121*, 1610–1630. [CrossRef]
15. de Laat, A.; Vazquez-Navarro, M.; Theys, N.; Stammes, P. Analysis of Properties of the 19 February 2018 Volcanic Eruption of Mount Sinabung in S5P/TROPOMI and Himawari-8 Satellite Data. *Nat. Hazards Earth Syst. Sci.* **2020**, *20*, 1203–1217. [CrossRef]
16. Prata, A.T.; Mingari, L.; Folch, A.; Macedonio, G.; Costa, A. FALL3D-8.0: A Computational Model for Atmospheric Transport and Deposition of Particles, Aerosols and Radionuclides—Part 2: Model Validation. *Geosci. Model Dev.* **2021**, *14*, 409–436. [CrossRef]
17. Pugnaghi, S.; Gangale, G.; Corradini, S.; Buongiorno, M.F. Mt. Etna Sulfur Dioxide Flux Monitoring Using ASTER-TIR Data and Atmospheric Observations. *J. Volcanol. Geotherm. Res.* **2006**, *152*, 74–90. [CrossRef]
18. Corradini, S.; Merucci, L.; Prata, A.J.; Piscini, A. Volcanic Ash and SO_2 in the 2008 Kasatochi Eruption: Retrievals Comparison from Different IR Satellite Sensors. *J. Geophys. Res.* **2010**, *115*, D00L21. [CrossRef]
19. Realmuto, V.J.; Berk, A. Plume Tracker: Interactive Mapping of Volcanic Sulfur Dioxide Emissions with High-Performance Radiative Transfer Modeling. *J. Volcanol. Geotherm. Res.* **2016**, *327*, 55–69. [CrossRef]
20. Kylling, A. Ash and Ice Clouds during the Mt Kelud February 2014 Eruption as Interpreted from IASI and AVHRR/3 Observations. *Atmos. Meas. Tech.* **2016**, *9*, 2103–2117. [CrossRef]
21. Carn, S.A. Quantifying Tropospheric Volcanic Emissions with AIRS: The 2002 Eruption of Mt. Etna (Italy). *Geophys. Res. Lett.* **2005**, *32*, L02301. [CrossRef]

22. Corradini, S.; Guerrieri, L.; Brenot, H.; Clarisse, L.; Merucci, L.; Pardini, F.; Prata, A.J.; Realmuto, V.J.; Stelitano, D.; Theys, N. Tropospheric Volcanic SO_2 Mass and Flux Retrievals from Satellite. The Etna December 2018 Eruption. *Remote Sens.* **2021**, *13*, 2225. [CrossRef]
23. Carn, S.A.; Krueger, A.J.; Bluth, G.J.S.; Schaefer, S.J.; Krotkov, N.A.; Watson, I.M.; Datta, S. Volcanic Eruption Detection by the Total Ozone Mapping Spectrometer (TOMS) Instruments: A 22-Year Record of Sulphur Dioxide and Ash Emissions. *Geol. Soc.* **2003**, *213*, 177–202. [CrossRef]
24. Elissavet, M.; Clarisse, L.; Carboni, N.E.; Gent, V.; Spinetti, N.C.; Balis, N.D.; Dimopoulos, N.S.; Grainger, N.D.; Theys, N.N.; Tampellini, L.; et al. Intercomparison of Metop-A SO_2 Measurements during the 2010- 2011 Icelandic Eruptions. *Ann. Geophys.* **2015**, *57*. [CrossRef]
25. Flemming, J.; Inness, A. Volcanic Sulfur Dioxide Plume Forecasts Based on UV Satellite Retrievals for the 2011 Grímsvötn and the 2010 Eyjafjallajökull Eruption. *J. Geophys. Res. Atmos.* **2013**, *118*, 10,172–10,189. [CrossRef]
26. Fedkin, N.M.; Li, C.; Krotkov, N.A.; Hedelt, P.; Loyola, D.G.; Dickerson, R.R.; Spurr, R. Volcanic SO_2 Effective Layer Height Retrieval for the Ozone Monitoring Instrument (OMI) Using a Machine-Learning Approach. *Atmos. Meas. Tech.* **2021**, *14*, 3673–3691. [CrossRef]
27. Grandin, R.; Boichu, M.; Mathurin, T.; Pascal, N. Automatic Estimation of Daily Volcanic Sulfur Dioxide Gas Flux from TROPOMI Satellite Observations: Application to Etna and Piton de La Fournaise. *J. Geophys. Res. Solid Earth* **2024**, *129*, e2024JB029309. [CrossRef]
28. Dozzo, M.; Aiuppa, A.; Bilotta, G.; Cappello, A.; Ganci, G. A New Algorithm for the Global-Scale Quantification of Volcanic SO_2 Exploiting the Sentinel-5P TROPOMI and Google Earth Engine. *Remote Sens.* **2025**, *17*, 534. [CrossRef]
29. Prata, A.J.; Kerkmann, J. Simultaneous Retrieval of Volcanic Ash and SO_2 using MSG-SEVIRI Measurements. *Geophys. Res. Lett.* **2007**, *34*, L05813. [CrossRef]
30. Corradini, S.; Merucci, L.; Prata, A.J. Retrieval of SO_2 from Thermal Infrared Satellite Measurements: Correction Procedures for the Effects of Volcanic Ash. *Atmos. Meas. Tech.* **2009**, *2*, 177–191. [CrossRef]
31. Prata, A.J.; Bernardo, C. Retrieval of Volcanic SO_2 column Abundance from Atmospheric Infrared Sounder Data. *J. Geophys. Res.* **2007**, *112*, D20204. [CrossRef]
32. EUMETSAT—SEVIRI Ash RGB Product Quick Guide. 2024. Available online: https://user.eumetsat.int/resources/user-guides/ash-rgb-quick-guide (accessed on 10 April 2024).
33. Torrisi, F.; Amato, E.; Corradino, C.; Mangiagli, S.; Del Negro, C. Characterization of Volcanic Cloud Components Using Machine Learning Techniques and SEVIRI Infrared Images. *Sensors* **2022**, *22*, 7712. [CrossRef]
34. Torrisi, F.; Corradino, C.; Cariello, S.; Del Negro, C. Enhancing detection of volcanic ash clouds from space with convolutional neural networks. *J. Volcanol. Geotherm. Res.* **2024**, *448*, 108046. [CrossRef]
35. Naranjo, C.; Corradini, S.; Guerrieri, L.; Stelitano, D.; Merucci, L.; Picchiani, M. Leveraging Machine Learning techniques and SEVIRI data to detect volcanic clouds composed of ash, ice, and SO_2 during the 2020–2022 Etna eruption activity. In Proceedings of the EGU General Assembly EGU25-10309, Vienna, Austria, 27 April–2 May 2025. [CrossRef]
36. Marchese, F.; Falconieri, A.; Filizzola, C.; Pergola, N.; Tramutoli, V. Investigating Volcanic Plumes from Mt. Etna Eruptions of December 2015 by Means of AVHRR and SEVIRI Data. *Sensors* **2019**, *19*, 1174. [CrossRef] [PubMed]
37. Theys, N.; Fioletov, V.; Li, C.; De Smedt, I.; Lerot, C.; McLinden, C.A.; Krotkov, N.A.; Griffin, D.C.; Clarisse, L.; Hedelt, P.; et al. A Sulfur Dioxide Covariance-Based Retrieval Algorithm (COBRA): Application to TROPOMI Reveals New Emission Sources. *Atmos. Chem. Phys.* **2021**, *21*, 16727–16744. [CrossRef]
38. Barker, A.K.; Troll, V.R.; Carracedo, J.C.; Nicholls, P.A. The Magma Plumbing System for the 1971 Teneguía Eruption on La Palma, Canary Islands. *Contrib. Mineral. Petrol.* **2015**, *170*, 54. [CrossRef]
39. Carracedo, J.C.; Badiola, E.R.; Guillou, H.; de la Nuez, J.; Torrado, F.J.P. Geology and Volcanology of La Palma and El Hierro, Western Canaries. *Estud. Geol.—Madr.* **2021**, *57*, 175–273. Available online: https://hal.science/hal-03323419 (accessed on 6 May 2025). [CrossRef]
40. Carracedo, J.C.; Troll, V.R.; Day, J.M.D.; Geiger, H.; Aulinas, M.; Soler, V.; Deegan, F.M.; Perez-Torrado, F.J.; Gisbert, G.; Gazel, E.; et al. The 2021 Eruption of the Cumbre Vieja Volcanic Ridge on La Palma, Canary Islands. *Geol. Today* **2022**, *38*, 94–107. [CrossRef]
41. De Luca, C.; Valerio, E.; Giudicepietro, F.; Macedonio, G.; Casu, F.; Lanari, R. Pre- and Co-Eruptive Analysis of the September 2021 Eruption at Cumbre Vieja Volcano (La Palma, Canary Islands) through DInSAR Measurements and Analytical Modeling. *Geophys. Res. Lett.* **2022**, *49*, e2021GL097293. [CrossRef]
42. Bonadonna, C.; Pistolesi, M.; Biass, S.; Voloschina, M.; Romero, J.; Coppola, D.; Folch, A.; D'Auria, L.; Martin-Lorenzo, A.; Dominguez, L.; et al. Physical Characterization of Long-Lasting Hybrid Eruptions: The 2021 Tajogaite Eruption of Cumbre Vieja (La Palma, Canary Islands). *J. Geophys. Res. Solid Earth* **2022**, *127*, e2022JB025302. [CrossRef]
43. Plan de Emergencias Volcánicas de Canarias. Available online: https://www.gobiernodecanarias.org/infovolcanlapalma/pevolca/ (accessed on 14 April 2024).

44. Esse, B.; Burton, M.; Hayer, C.; La Spina, G.; Pardo Cofrades, A.; Asensio-Ramos, M.; Barrancos, J.; Pérez, N. Forecasting the Evolution of the 2021 Tajogaite Eruption, La Palma, with TROPOMI/PlumeTraj-Derived SO_2 Emission Rates. *Bull. Volcanol.* **2025**, *87*, 20. [CrossRef]
45. EUMETSAT—MSG Services. 2024. Available online: https://www.eumetsat.int/msg-services (accessed on 15 May 2024).
46. Veefkind, J.; Claas, J.; Van Weele, M.; Aben, I.; Visser, H.; Kleipool, Q.; De Vries, J.; Vink, R.; Haan, J.; Förster, H.; et al. TROPOMI on the ESA Sentinel-5 Precursor: A GMES mission for global observations of the atmospheric composition for climate, air quality and ozone layer applications. *Remote Sens. Environ.* **2012**, *120*, 70–83. [CrossRef]
47. S5P-PAL Data Portal. Available online: https://data-portal.s5p-pal.com/products/so2cbr.html (accessed on 15 May 2024).
48. Tramutoli, V. Robust AVHRR Techniques (RAT) for Environmental Monitoring: Theory and Applications. *Proc. SPIE* **1998**, *110*. [CrossRef]
49. Tramutoli, V. Robust Satellite Techniques (RST) for Natural and Environmental Hazards Monitoring and Mitigation: Theory and Applications. In Proceedings of the International Workshop on Analysis of Multi-temporal Remote Sensing Images. In Proceedings of the 2007 International Workshop on the Analysis of Multi-temporal Remote Sensing Images, Leuven, Belgium, 18–20 July 2007; pp. 1–6. [CrossRef]
50. Pergola, N.; Coviello, I.; Filizzola, C.; Lacava, T.; Marchese, F.; Paciello, R.; Tramutoli, V. A Review of RSTVOLC, an Original Algorithm for Automatic Detection and Near-Real-Time Monitoring of Volcanic Hotspots from Space. *Geol. Soc.* **2015**, *426*, 55–72. [CrossRef]
51. Pergola, N.; Tramutoli, V.; Marchese, F.; Scaffidi, I.; Lacava, T. Improving Volcanic Ash Cloud Detection by a Robust Satellite Technique. *Remote Sens. Environ.* **2004**, *90*, 1–22. [CrossRef]
52. Marchese, F.; Filizzola, C.; Mazzeo, G.; Pergola, N.; Sannazzaro, F.; Tramutoli, V. Assessment and Validation in Time Domain of a Robust Satellite Technique (RST_{ASH}) for Ash Cloud Detection. *Geomat. Nat. Hazards Risk* **2011**, *2*, 247–262. [CrossRef]
53. Piscini, A.; Corradini, S.; Marchese, F.; Merucci, L.; Pergola, N.; Tramutoli, V. Volcanic Ash Cloud Detection from Space: A Comparison between the RSTASH Technique and the Water Vapour Corrected BTD Procedure. *Geomat. Nat. Hazards Risk* **2011**, *2*, 263–277. [CrossRef]
54. Marchese, F.; Falconieri, A.; Pergola, N.; Tramutoli, V. Monitoring the Agung (Indonesia) Ash Plume of November 2017 by Means of Infrared Himawari 8 Data. *Remote Sens.* **2018**, *10*, 919. [CrossRef]
55. Falconieri, A.; Cooke, M.; Filizzola, C.; Marchese, F.; Pergola, N.; Tramutoli, V. Comparing Two Independent Satellite-Based Algorithms for Detecting and Tracking Ash Clouds by Using SEVIRI Sensor. *Sensors* **2018**, *18*, 369. [CrossRef]
56. Marchese, F.; Falconieri, A.; Pergola, N.; Tramutoli, V. A Retrospective Analysis of the Shinmoedake (Japan) Eruption of 26–27 January 2011 by Means of Japanese Geostationary Satellite Data. *J. Volcanol. Geotherm. Res.* **2014**, *269*, 1–13. [CrossRef]
57. Marchese, F.; Ciampa, M.; Filizzola, C.; Lacava, T.; Mazzeo, G.; Pergola, N.; Tramutoli, V. On the Exportability of Robust Satellite Techniques (RST) for Active Volcano Monitoring. *Remote Sens.* **2010**, *2*, 1575–1588. [CrossRef]
58. Falconieri, A.; Papagiannopoulos, N.; Marchese, F.; Filizzola, C.; Trippetta, S.; Pergola, N.; Pappalardo, G.; Tramutoli, V.; Mona, L. Validation of Ash/Dust Detections from SEVIRI Data Using ACTRIS/EARLINET Ground-Based LIDAR Measurements. *Remote Sens.* **2020**, *12*, 1172. [CrossRef]
59. Prata, A.J. Infrared Radiative Transfer Calculations for Volcanic Ash Clouds. *Geophys. Res. Lett.* **1989**, *16*, 1293–1296. [CrossRef]
60. Ellrod, G.P. Improved Detection of Airborne Volcanic Ash Using Multispectral Infrared Satellite Data. *J. Geophys. Res.* **2003**, *108*. [CrossRef]
61. Koeppen, W.C.; Pilger, E.; Wright, R. Time Series Analysis of Infrared Satellite Data for Detecting Thermal Anomalies: A Hybrid Approach. *Bull. Volcanol.* **2010**, *73*, 577–593. [CrossRef]
62. Cuomo, V.; Filizzola, C.; Pergola, N.; Pietrapertosa, C.; Tramutoli, V. A Self-Sufficient Approach for GERB Cloudy Radiance Detection. *Atmos. Res.* **2004**, *72*, 39–56. [CrossRef]
63. Grandini, M.; Bagli, E.; Visani, G. Metrics for Multi-Class Classification: An Overview. *arXiv* **2020**, arXiv:2008.05756. [CrossRef]
64. Milford, C.; Torres, C.; Vilches, J.; Gossman, A.-K.; Weis, F.; Suárez-Molina, D.; García, O.E.; Prats, N.; Barreto, Á.; García, R.D.; et al. Impact of the 2021 La Palma Volcanic Eruption on Air Quality: Insights from a Multidisciplinary Approach. *Sci. Total Environ.* **2023**, *869*, 161652. [CrossRef]
65. SACS—Support to Aviation Control Service. Available online: http://sacs.aeronomie.be/ (accessed on 10 April 2024).
66. Kearney, C.S.; Watson, I.M. Correcting Satellite-Based Infrared Sulfur Dioxide Retrievals for the Presence of Silicate Ash. *J. Geophys. Res. Atmos.* **2009**, *114*, D22208. [CrossRef]
67. Theys, N.; Hedelt, P.; De Smedt, I.; Lerot, C.; Yu, H.; Vlietinck, J.; Pedergnana, M.; Arellano, S.; Galle, B.; Fernandez, D.; et al. Global Monitoring of Volcanic SO_2 Degassing with Unprecedented Resolution from TROPOMI Onboard Sentinel-5 Precursor. *Sci. Rep.* **2019**, *9*, 2643. [CrossRef]

68. De Santis, D.; Petracca, I.; Corradini, S.; Guerrieri, L.; Picchiani, M.; Merucci, L.; Stelitano, D.; Del Frate, F.; Prata, F.; Schiavon, G. Volcanic SO_2 near-real time retrieval using TROPOMI data and neural networks: The December 2018 Etna test case. In Proceedings of the 2021 IEEE International Geoscience and Remote Sensing Symposium IGARSS, Brussels, Belgium, 11–16 July 2021; pp. 8480–8483.
69. Corradino, C.; Jouve, P.; La Spina, A.; Del Negro, C. Monitoring Earth's atmosphere with Sentinel-5 TROPOMI and Artificial Intelligence: Quantifying volcanic SO_2 emissions. *Remote Sens. Environ.* **2024**, *315*, 114463. [CrossRef]
70. VAAC—Volcanic Ash Advisory Center of Tolouse. Available online: https://vaac.meteo.fr/volcanoes/la-palma/page/19/ (accessed on 14 May 2024).
71. Filizzola, C.; Mazzeo, G.; Marchese, F.; Pietrapertosa, C.; Pergola, N. The Contribution of Meteosat Third Generation–Flexible Combined Imager (MTG-FCI) Observations to the Monitoring of Thermal Volcanic Activity: The Mount Etna (Italy) February–March 2025 Eruption. *Remote Sens.* **2025**, *17*, 2102. [CrossRef]